JOURNAL OF CATALYSIS **171,** 457–466 (1997)
ARTICLE NO. CA971826

Characterization of Pt/SbO_x Catalysts Active for Selective Oxidation of Isobutane by Means of XRD, TEM, and XAFS

Tomoya Inoue,* Kiyotaka Asakura,† and Yasuhiro Iwasawa*,[1]

*Department of Chemistry, †Research Center for Spectrochemistry, Graduate School of Science, The University of Tokyo, 7-3-1 Hongo, Bunkyo-ku, Tokyo 113, Japan

Received March 4, 1997; revised July 1, 1997; accepted July 11, 1997

New Pt/SbO_x catalysts active for the selective oxidation of i-C_4H_{10} and i-C_4H_8 were characterized by means of XRD, TEM, and XAFS as well as H_2 and CO adsorption. Pt was present as metallic particles, while SbO_x existed as Sb_6O_{13} phase. It was suggested that the surface layer of the Pt particles was modified with SbO_y ($y < x$) under the i-C_4H_{10} and i-C_4H_8 selective oxidation reaction conditions at 773 K. This modification of Pt particles by SbO_y induces high selectivity to MAL in both i-C_4H_{10} and i-C_4H_8 oxidation reactions. Activation of i-C_4H_{10} (i-C_4H_{10} dehydrogenation) is suggested to occur on the Pt–SbO_y sites in the presence of oxygen, while the Sb_6O_{13} phase is responsible for selective oxidation of dehydrogenated intermediates. The degree of the Sb modification depends on the reaction conditions. When the Pt/SbO_x catalyst was reduced with H_2 at 473 K, Pt–Sb alloy particles (Pt–Pt = 0.274 nm and Pt–Sb = 0.260 nm) were formed, and the Sb_6O_{13} was partly reduced to α-Sb_2O_4. This heavily reduced state of the surface was nonselective for the i-C_4H_{10} oxidation.

INTRODUCTION

The functionalization of small alkanes using gas phase oxygen has been extensively studied from fundamental and industrial points of view. Activation of small alkanes is usually achieved under more severe reaction conditions compared with those for the corresponding alkenes, which decreases the selectivity to the desired partially oxidized species. Better performance in the selective oxidation may be possible on a new type of catalytic system, which can activate the alkanes in mild conditions (1, 2).

To date multicomponent oxide catalysts have been developed, but the lower yield and/or selectivity, catalyst life, and reaction conditions have prevented them from being used in practical processes. The only successful example is the *n*-butane oxidation to maleic acid anhydride by V–P–O catalysts (3).

Unsaturated nitriles and aldehydes which are important basic chemicals have been produced by oxidation or ammoxidation of propene or isobutylene (4, 5). Increasing demand for the use of alkanes, rather than alkenes, as starting materials for their syntheses tempted us to explore a new catalytic system for the selective oxidation of small alkanes. Some catalysts have been found promising in the selective oxidation processes starting from alkanes. V–Sb–O-based catalysts have been developed to the level of pilot plant use (1, 6). Scheelite-type Bi–V–O has been reported to work as a good catalyst for propane oxidation or ammoxidation to acrolein or acrylonitrile (7). Recently, V–Mo–Nb–Te oxide catalysts have been reported to be active and selective for propane ammoxidation to acrylonitrile at lower temperatures, compared to the case of the V–Sb–O and Bi–V–O catalysts (8–10). Despite these exploits, further improvement on catalytic performance and catalyst life is needed.

Activation of the C–H bond in alkanes (C–H bond dissociation) has been demonstrated as a key issue for the alkane selective oxidation reactions. Noble metals such as Pt, Pd, and Rh may be candidates for active elements for the dehydrogenation of alkane molecules at relatively low temperatures. However, they are also good catalysts for the complete oxidation of alkanes to CO_2, which is a reason that supported noble metals have not been employed as selective oxidation catalysts. It is possible to control the property of the noble metals by addition of the second metal and to create new catalysis by the obtained noble metal-additive metal ensembles. In fact, it was found that the Pt–Sn ensembles on SiO_2 catalyzed the synthesis of unsaturated nitriles from NO and isobutane with a good selectivity of 70% (11, 12).

Recently, we have found that Pt/SbO_x catalysts were active for the isobutane (i-C_4H_{10}) oxidation to methacrolein (MAL) with a high selectivity of 57%, and the selectivity including the intermediate isobutylene (i-C_4H_8) was as high as 90%. SbO_x never produced MAL from i-C_4H_{10}, while i-C_4H_8 was converted to MAL with a high selectivity on the SbO_x, the yield of MAL in the i-C_4H_8 oxidation also increasing seven times by the coexistence of Pt. Temperature-programmed reaction profiles in the i-C_4H_8 oxidation on Pt/SbO_x catalysts indicated that some modification

[1] Corresponding author. Fax: 81-3-5800-6892. E-mail: iwasawa@chem.s.u-tokyo.ac.jp.

0021-9517/97 $25.00

occurred on the Pt particles under the reaction conditions, which seemed responsible for the high selectivity to MAL (13, 14). Performance of the Pt/SbO_x catalyst in the i-C_4H_{10} and i-C_4H_8 selective oxidation will be reported separately (15).

The aim of this paper is to examine the state of Pt in Pt/SbO_x, the state of the Sb oxide, and the interaction of Pt and SbO_x, which may be relevant to the good performance of the new Pt/SbO_x system for the selective oxidation of i-C_4H_{10} and i-C_4H_8 to MAL. We have studied these issues by means of XRD, TEM, and XAFS (X-ray absorption fine structure), and gas adsorption. These techniques will provide complementary information with each other about the structure and state of Pt in Pt/SbO_x.

EXPERIMENTAL

Catalyst Preparation

Antimony oxide (SbO_x) was prepared by hydrolytic precipitation of an aqueous solution of $SbCl_5$ with an aqueous ammonia solution followed by drying at 373 K and calcination at 773 K. The obtained Sb oxide was impregnated by an acetone solution of $Pt(acac)_2$, followed by drying at 323 K and calcination at 773 K. The precursors $SbCl_5$ and $Pt(acac)_2$ were purchased from Soekawa Chemical Co. and used without further purification.

Characterization of Catalysts

1. Adsorption measurements. The amounts of adsorbed H_2 (Takachiho Chemical Co., purity 99.9999%) and CO (Takachiho Chemical Co., purity 99.95%) on Pt/SbO_x catalysts were measured volumetrically in a closed circulating system (dead volume: 70 cm^3). The amount of irreversible adsorption was estimated by subtracting the amount of reversible adsorption obtained at the second adsorption experiment from the adsorbed amount determined from the first adsorption measurement.

The Pt/SbO_x catalysts were not reduced with H_2 before the adsorption measurements because the H_2 reduction treatment changed the surface state of the catalysts (13, 15). Instead, the catalysts were calcined at 773 K and evacuated at 473 K. The samples thus treated were subjected to the adsorption experiment.

2. XRD measurements. Powder XRD patterns were obtained on a Geigerflex diffractometer (Rigaku) using Cu $K\alpha_1$ radiation ($\lambda = 0.15418$ nm). Crystalline phases were identified using ASTM files.

Pt particle size on average (L) was estimated by the linewidth of Pt(111) diffraction peak (16),

$$L = K\lambda/\Delta(2\theta)\cos\theta_0, \qquad [1]$$

where λ represents wavelength of Cu $K\alpha_1$ radiation, and K is a constant (0.89–1.39, depending on the sample), where K was fixed to 1. $\Delta(2\theta)$ and θ_0 stand for diffraction line width and diffraction angle, respectively.

3. TEM measurements. Transmission electron microscope (TEM) photographs for determination of mean metal particle sizes in Pt/SbO_x catalysts (Pt: 0.5 and 2.0 wt%) were taken on a JEM 2010/LaB_6 microscope (JEOL). The samples were stored in ampoules until TEM measurements and exposed to atmosphere at room temperature just before TEM measurements.

The TEM photographs were taken with 350,000 magnification and more than 500 metallic particles were scaled for every sample to get the particle size distribution. The averaged particle size (diameter) ($\overline{d}$) was defined by Eq. [2] (17):

$$\overline{d} = \sum_i n_i d_i^3 \Big/ \sum_i n_i d_i^2. \qquad [2]$$

4. XAFS measurements and analysis. Pt L_{III}-edge XAFS spectra for Pt/SbO_x catalysts were measured at the BL-7C of the Photon Factory in the National Laboratory for High Energy Physics (KEK-PF) with a storage-ring energy of 2.5 GeV and a maximum current of 350 mA (Proposal No. 95G002). A synchrotron radiation was monochromatized by a Si(111) sagital focusing double crystal. Higher harmonics were removed by detuning the parallelism for the intensity to be 60% of the maximum. Pt L_{III}-edge spectra were recorded in a transmission mode using ionization chambers filled with N_2 for I_0 and filled with Ar 15% + N_2 85% for I. In EXAFS analysis, Sb has a large X-ray absorption in the Pt L_{III}-edge EXAFS region which makes it difficult to measure EXAFS spectra with a good S/B ratio for the Pt/SbO_x samples with low loading of Pt in a transmission mode. Hence, the EXAFS spectra for 0.5 wt% Pt/SbO_x were taken by a fluorescence method. For the fluorescence mode a Lytle detector filled with Ar was used.

The catalyst samples were prepared in a fixed-bed flow reactor to which glass-made XAFS cells with kapton windows were connected, and the samples were transferred to the XAFS cells under the preparation atmosphere without contacting air.

The EXAFS data were analyzed by the EXAFS analysis program "REX" (Rigaku). The analysis involves preedge extrapolation, background removal by a cubic spline method to extract EXAFS oscillation, and Fourier transformation from k space to R space using a Hanning window function with 1/10 of the Fourier transform range. Inversely Fourier transformed data from R space to k space were analyzed by a curve-fitting method to obtain detailed structural information.

We used the EXAFS formula (Eq. [3]) based on a single scattering theory in the curve-fitting analysis of the EXAFS

data (18, 19)

$$\chi(k'_j) = \sum_j N_j F(k'_j) \exp(-2k'^2_j\sigma^2_j) \sin(2k'_j R_j + \phi(k'_j))/k'_j R^2_j \quad [3]$$

$$k'_j = (k^2_j - 2m\Delta E_{0j}/h^2)^{1/2}, \quad [4]$$

where k_j and ΔE_{0j} are the photoelectron wavenumber and the difference between the origin of the photoelectron wavenumber and that conventionally determined, respectively. $F(k'_j)$ is the backscattering amplitude function and $\phi(k'_j)$ is the phase shift function. N_j, σ_j, and R_j are the coordination number, the Debye–Waller factor, and the interatomic distance, respectively. The fitting parameters are N_j, σ_j, R_j, and ΔE_{0j}. The curve fitting results for the k^3-weighted EXAFS data were evaluated by the residual factor, denoted by R_f, which is calculated as

$$R_f = \int_{k_{\min}}^{k_{\max}} |k^3\chi^{\text{obs}}(k) - k^3\chi^{\text{calc}}(k)|^2 dk \Big/ \int_{k_{\min}}^{k_{\max}} |k^3\chi^{\text{obs}}(k)|^2 dk. \quad [5]$$

Since no good reference compound was available for Pt–Sb in Pt L_{III}-edge EXAFS analysis, theoretical parameters derived from FEFF 6.01 were used for the backscattering amplitude and phase shift functions for Pt–Sb bond (20). The backscattering amplitude and phase shift functions for Pt–Pt bond parameters were extracted from the EXAFS data for Pt foil. The EXAFS analysis was performed by taking into account the number of the independent parameters (N_I) given by Eq. [6] (19, 21),

$$N_I = (2\Delta R\Delta k/\pi) + n \quad (n = 0, 1), \quad [6]$$

where ΔR and Δk denote the Fourier filtering range for the curve-fitting analysis and the Fourier transform range for $k^3\chi(k)$, respectively.

RESULTS

H_2 and CO Adsorption

After the calcination of Pt/SbO_x at 773 K, the surface area was estimated to be 58 $m^2\ g^{-1}$ by the BET method, and it remained unchanged after repeated *i*-C_4H_{10} oxidation reaction, 52 $m^2\ g^{-1}$. The surface area was independent of Pt loading (0–2.0 wt%), except for too heavily reduced samples. All samples examined in this study had similar surface areas, 50–60 $m^2\ g^{-1}$.

Because the surface of Pt particles in Pt/SbO_x may be partly covered with oxygen after the calcination at 773 K, the stoichiometric reaction, Pt–O + 3H → Pt–H + H_2O, was assumed to evaluate the amount of adsorbed H. The amount of adsorbed H determined by this equation was compared to that determined by readsorption measurement of hydrogen after evacuation of the H-adsorbed surface at 473 K for 1 h (Table 1). The first adsorption conducted after the calcination at 773 K shows H/Pt = 0.24 for Pt(2.0 wt%)/SbO_x. The readsorbed measurement showed the similar H/Pt value, 0.29. The agreement of H/Pt in the two adsorption measurements within experimental errors was also observed for the samples with 0.5 wt% and 1.0 wt% Pt loadings. By using these H/Pt values, Pt particle sizes were estimated to be 13 nm for 0.5 wt% Pt/SbO_x, 12 nm for 1.0 wt% Pt/SbO_x, and 5.2 nm for 2.0 wt% Pt/SbO_x. After the first hydrogen adsorption, the sample was evacuated at 473 K for 1 h, then CO was adsorbed at room temperature. The results are also given in Table 1. The amount of adsorbed CO was much smaller than that of adsorbed H on the Pt/SbO_x catalysts.

Table 2 shows the results of adsorption measurements on the samples after H_2 reduction at 473 K and the selective oxidation reactions of *i*-C_4H_{10} and *i*-C_4H_8 at 773 K. After the reduction and reactions the amounts of adsorbed hydrogen remarkably reduced to negligible levels.

TABLE 1

H/Pt and CO/Pt for Pt/SbO_x and Pt/Al_2O_3 Catalysts[a] Calcined at 773 K

Pt/SbO_x	H/Pt (first)[b]	H/Pt (second)[c]	CO/Pt
0.5 wt% Pt	0.07	0.06	0.00
1.0 wt% Pt	0.08	0.14	0.03
2.0 wt% Pt	0.24	0.29	0.04
Pt/Al_2O_3 (5.0 wt%)	0.47	0.44	0.44

Note. T_{ads} = 273 K; P_{H_2} or P_{CO} = 13.3 kPa.

[a] Pt/Al_2O_3 was used as a reference sample to examine the adsorption property of Pt/SbO_x samples.

[b] Assuming Pt–O + 3H → Pt–H + H_2O.

[c] After evacuation of the Pt–H sample (first adsorption) at 473 K.

TABLE 2

H/Pt and CO/Pt for Pt/SbO_x Catalysts after H_2 Reduction at 473 K and Selective Oxidation Reactions of *i*-C_4H_{10} and *i*-C_4H_8 at 773 K

Pt/SbO_x	H/Pt[a]	CO/Pt
0.5 wt%		
H_2 red. at 473 K	0.00	0.02
2.0 wt%		
H_2 red. at 473 K	0.00	0.00
i-C_4H_{10} ox. at 773 K	0.01	0.00
i-C_4H_8 ox. at 773 K	0.01	—

Note. Selective oxidation reaction conditions: 2400 ml h^{-1}; 20% *i*-C_4H_{10} or 1.7% *i*-C_4H_8; 4% O_2, balanced with He. T_{ads} = 273 K; P_{H_2} or P_{CO} = 13.3 kPa.

[a] Assuming Pt–O + 3H → Pt–H + H_2O.

XRD

Figure 1 shows XRD patterns for the Pt/SbO_x catalysts with 0.5 wt% and 2.0 wt% Pt loadings after calcination at 773 K, *i*-C_4H_{10} oxidation at 773 K, *i*-C_4H_8 oxidation at 773 K, and reduction with H_2 at 473 K. The Pt(111) peak observed with Pt (0.5 wt%)/SbO_x calcined at 773 K reveals that Pt metallic particles were formed after the calcination. The shape of the Pt(111) diffraction peak remained unchanged after the *i*-C_4H_{10} oxidation reaction at 773 K. In contrast, the peak intensity markedly decreased after the *i*-C_4H_8 oxidation reaction (4% *i*-C_4H_8, 4% O_2, balanced with He) at 773 K. Similar reduction in the Pt(111) peak intensity was observed with the sample which was reduced with H_2 at 473 K.

The Pt particle size was estimated from the full width at half maximum of the Pt(111) diffraction peak although the XRD patterns were noisy due to low loadings of Pt. The mean diameters of Pt particles were 6.4 nm for Pt/SbO_x (0.5 wt%) and 3.5 nm for 2.0 wt%. It is to be noted that these values were almost half as large as those estimated from the hydrogen adsorption. Another issue to be noted is that after the *i*-C_4H_{10} oxidation reaction, XRD showed little change in the Pt(111) diffraction peak, indicating almost no aggregation of Pt particles to large particles, while the adsorption of hydrogen reduced to nearly zero.

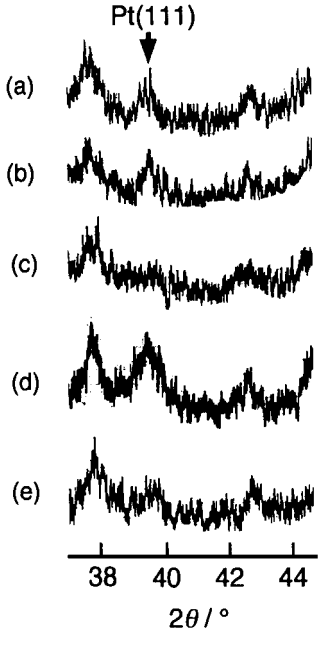

FIG. 1. XRD patterns for crystalline Pt particles in Pt/SbO_x catalysts: (a) Pt/SbO_x (0.5 wt%) calcined at 773 K; (b) Pt/SbO_x (0.5 wt%) after *i*-C_4H_{10} selective oxidation reaction at 773 K in a fixed-bed flow reactor, catal. weight = 0.3 g, total flow rate = 2400 ml h^{-1}, *i*-C_4H_{10} = 20%, O_2 = 4%, balanced with He; (c) Pt/SbO_x (0.5 wt%) after *i*-C_4H_8 selective oxidation reaction at 773 K, *i*-C_4H_8 = 4%, O_2 = 4%, balanced with He; (d) Pt/SbO_x (2.0 wt%) calcined at 773 K; (e) Pt/SbO_x (2.0 wt%) reduced with H_2 at 473 K in a closed circulating system.

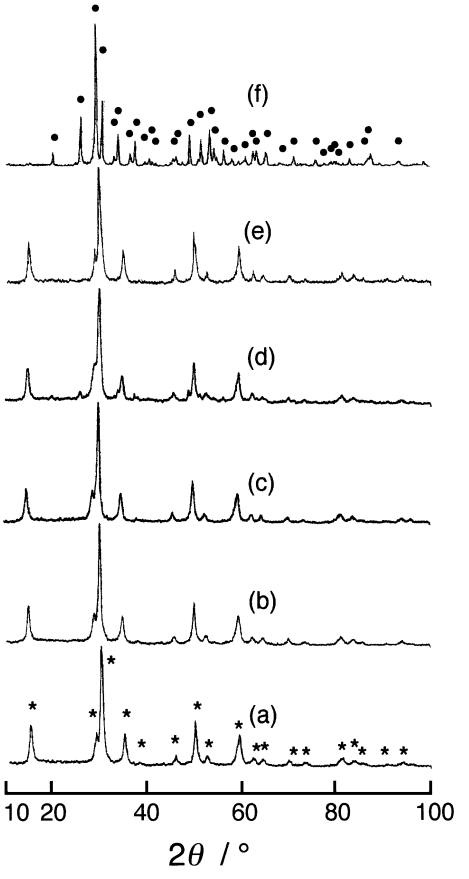

FIG. 2. XRD patterns for SbO_x and Pt/SbO_x: (a) SbO_x after calcination at 773 K (∗: assigned to Sb_6O_{13}); (b) SbO_x after *i*-C_4H_8 selective oxidation at 773 K (1.7% *i*-C_4H_8, 4% O_2, balanced with He); (c) Pt/SbO_x (2.0 wt%) after *i*-C_4H_8 selective oxidation at 698 K (1.7% *i*-C_4H_8, 4% O_2, balanced with He); (d) Pt/SbO_x (2.0 wt%) after *i*-C_4H_8 selective oxidation at 773 K (1.7% *i*-C_4H_8, 4% O_2, balanced with He); (e) Pt/SbO_x (0.5 wt%) after *i*-C_4H_{10} selective oxidation at 773 K (20% *i*-C_4H_{10}, 4% O_2, balanced with He), (f) Pt/SbO_x (0.5 wt%) after *i*-C_4H_8 oxidation under the *i*-C_4H_8 rich (20%) condition at 773 K (20% *i*-C_4H_8, 4% O_2, balanced with He) followed by *i*-C_4H_{10} oxidation at 773 K (20% *i*-C_4H_{10}, 4% O_2, balanced with He) (●: assigned to α-Sb_2O_4). The *i*-C_4H_{10} and *i*-C_4H_8 oxidation were conducted in a fixed-bed flow reactor using 0.3 g catalyst at a total flow rate of 2400 ml h^{-1} and an atmospheric pressure.

Powder XRD patterns in the wide range of 2θ for Pt/SbO_x and SbO_x samples are shown in Fig. 2. The SbO_x phase in all samples except for sample (f) was identified as Sb_6O_{13}. The SbO_x sample without Pt always comprised of Sb_6O_{13} alone irrespective of the calcination and the *i*-C_4H_{10} and *i*-C_4H_8 oxidation at 773 K. The Pt/SbO_x catalyst after *i*-C_4H_{10} oxidation at 773 K also constituted the Sb_6O_{13} phase (Fig. 2e). However, the Sb_6O_{13} structure was partly converted to α-Sb_2O_4 when *i*-C_4H_8 oxidation was performed on Pt (2.0 wt%)/SbO_x (Fig. 2d). In this case the combustion to CO_2 was enhanced. The α-Sb_2O_4 phase became major with the Pt/SbO_x after *i*-C_4H_8 oxidation under the *i*-C_4H_8-rich (20%) reaction condition as shown in Fig. 2f. The selectivity to MAL in the *i*-C_4H_{10} and *i*-C_4H_8 oxidation reactions

on this phase became nearly zero and the total oxidation to CO_2 was predominant.

XAFS

Figures 3A and B show the Pt L_{III}-edge XANES spectra for Pt/SbO_x with 0.5 wt% and 2.0 wt% Pt, respectively. The white line intensity of Pt/SbO_x after calcination was larger than that for Pt foil, which may be due to the adsorbed oxygen on the Pt surface of the calcined catalyst. It coincides with our assumption made in the calculation of adsorbed hydrogen. The white line intensities of the XANES spectra for Pt/SbO_x after *i*-C_4H_{10} and *i*-C_4H_8 oxidation reactions decreased to the same level as that for Pt foil. By H_2 reduction at 473 K, the peak height of the white line was similar to that for Pt foil, but the peak became broader, suggesting modification of the electronic state of Pt particles.

Figure 4 shows the Pt L_{III}-edge EXAFS oscillations for the Pt/SbO_x catalysts with Pt loadings of 0.5 wt% (A) and 2.0 wt% (B), which are the same samples as those in Fig. 3. The EXAFS oscillations of both Pt/SbO_x catalysts after calcination resemble that of bulk Pt, and the oscillations remained essentially unchanged after the *i*-C_4H_{10} and *i*-C_4H_8 selective oxidation reactions at 773 K. These results also indicate that the Pt atoms in Pt/SbO_x are present as metallic particles, independently of calcination and reactions. The oscillations for Pt foil, Pt/SbO_x calcined at 773 K, and Pt/SbO_x after *i*-C_4H_8 oxidation (1.7% *i*-C_4H_8, 4% O_2, balanced with He) at 773 K were also Fourier transformed in Fig. 4. The Fourier transforms for these samples also reveal Pt particles in the metallic state with these samples.

As for the Pt/SbO_x (0.5 and 2.0 wt%) after *i*-C_4H_{10} oxidation at 773 K, the EXAFS data were analyzed by a curve-fitting technique in Fig. 5, which shows the oscillations, their Fourier transforms and curve-fitting analyses. The one-shell (Pt–Pt) curve fitting almost completely reproduced the observed data as shown in Figs. 5Ac and 5Bc. The coordination numbers for Pt–Pt determined by EXAFS were 10.3 (0.5 wt% Pt/SbO_x) and 11.8 (2.0 wt% Pt/SbO_x) (Table 3). These values indicate that these Pt particles are larger than 4.0 nm (22).

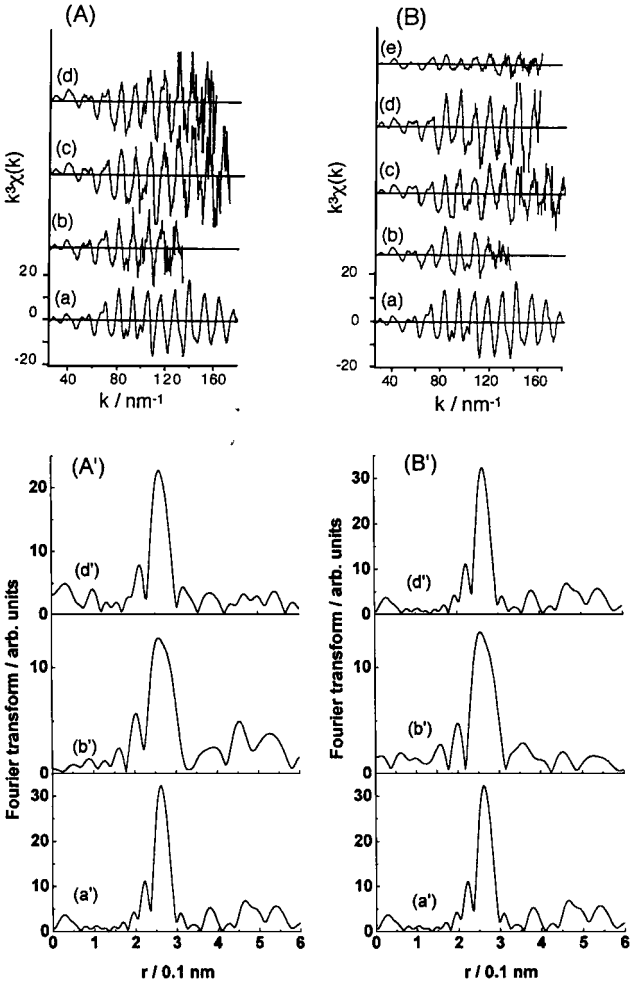

FIG. 4. Pt L_{III}-edge EXAFS oscillations ($k^3\chi(k)$) and their associated Fourier transforms for 0.5 wt% Pt/SbO_x (A and A′) and 2.0 wt% Pt/SbO_x (B and B′); (a)–(e), same samples as in Fig. 3.

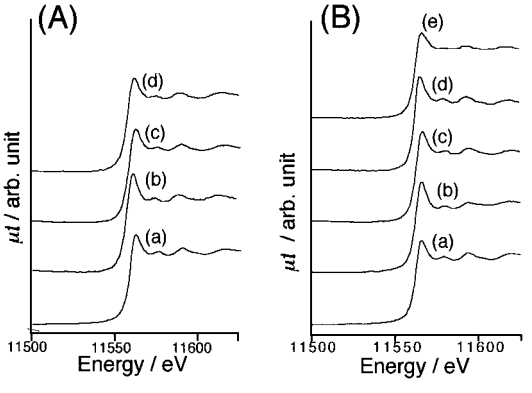

FIG. 3. Pt L_{III}-edge XANES spectra of 0.5 wt% Pt/SbO_x (A) and 2.0 wt% Pt/SbO_x (B): (a) Pt foil as a reference; (b) after calcination at 773 K; (c) after *i*-C_4H_{10} selective oxidation at 773 K (20% *i*-C_4H_{10}, 4% O_2, balanced with He); (d) after *i*-C_4H_8 selective oxidation at 773 K (1.7% *i*-C_4H_8, 4% O_2, balanced with He); (e) after H_2 reduction at 473 K.

When the 2.0 wt% Pt/SbO_x catalyst was reduced with H_2 at 473 K, the EXAFS oscillation in Fig. 4Be drastically reduced compared with the others in Fig. 4. Figure 6a reproduces the EXAFS oscillation of Figs. 4Be, and 6b, c, and d are its associated Fourier transform, one-shell (Pt–Pt) curve-fitting, and two-shells (Pt–Pt and Pt–Sb) curve-fitting, respectively. The amplitude of oscillation is as weak as one-third of that for Pt foil. To obtain the structural information on bond distance and coordination number, we performed the curve-fitting analysis assuming Pt–Pt in Fig. 6c. The one-shell (Pt–Pt) fitting (*R* factor: 7.8%) never reproduced the EXAFS data. Then we performed two-shell fitting, assuming Pt–Pt and Pt–Sb bonding. The best-fit result is shown

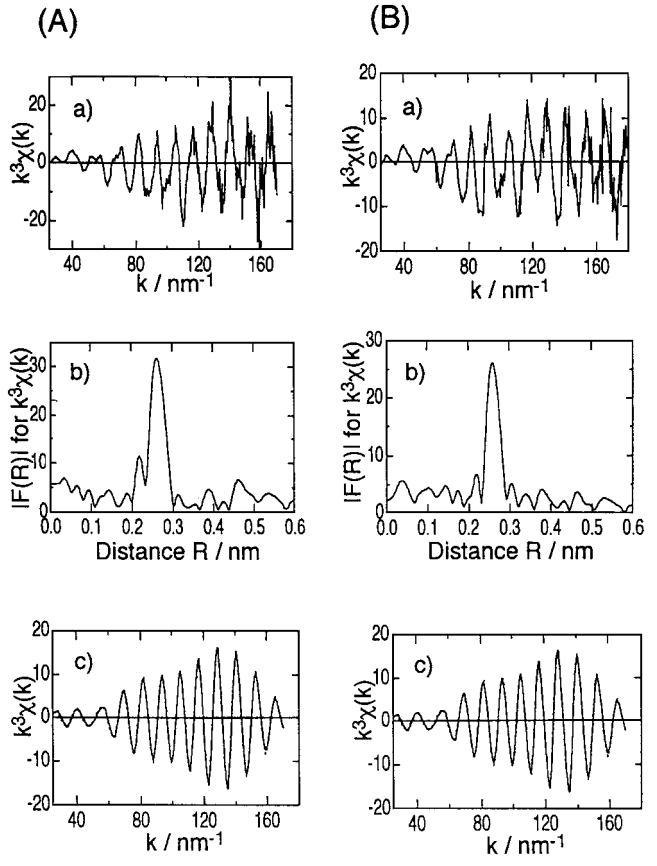

FIG. 5. EXAFS oscillations, Fourier transforms, and curve-fittings for 0.5 wt% Pt/SbO_x (A) and 2.0 wt% Pt/SbO_x (B) after *i*-C_4H_{10} selective oxidation at 773 K (20% *i*-C_4H_{10}, 4% O_2, balanced with He).

in Fig. 6d, where the fitted curve coincides well with the experimental data. The interatomic distances and coordination numbers for Pt–Pt and Pt–Sb were determined to be 0.274 nm and 6.1, and 0.260 nm and 0.6, respectively (Table 3). Thus the H_2 reduction produces the Pt–Sb alloy particles on the Sb oxide surface. The decrease in the coordination number of Pt–Pt may be due to large disorder induced by the formation of Pt–Sb bond. Similar reduction in the coordination number has also been observed in Pt–Sn and Rh–Sn particles (11, 12, 23, 24).

TEM

Figures 7a and b show the TEM photographs for the calcined Pt/SbO_x catalysts with Pt loadings of 0.5 and 2.0 wt%, respectively. Antimony oxide was easily damaged by electron beams and readily sublimated during the TEM observation. Consequently, the part of SbO_x support in Pt/SbO_x gave thin contrast, while Pt particles were observed as black contrast. Beam damage of Pt particles was considered to be negligible when TEM is used as a tool to estimate averaged size of Pt metallic particles, because the size of each particle seemed unchanged during the TEM observation. The

TABLE 3

Curve-Fitting Results for the Pt L_{III}-Edge EXAFS Data of the 0.5 and 2.0 wt% Pt/SbO_x Catalysts after Calcination at 773 K and Selective Oxidation Reactions of *i*-C_4H_{10} and *i*-C_4H_8 at 773 K

	Bond	N^e	R/nm^f	ΔE_0/eV	D. W./nm^2	R_f/%
0.5 wt% Pt						
Calc.[a]	Pt–Pt	10.3	0.277	−0.7	4.4×10^{-5}	1.2
i-C_4H_{10} ox.[b]	Pt–Pt	11.7	0.277	−1.6	3.3×10^{-5}	0.4
i-C_4H_8 ox.[c]	Pt–Pt	10.9	0.276	−4.1	3.8×10^{-5}	1.9
2 wt% Pt						
Calc.[a]	Pt–Pt	11.8	0.275	−4.4	5.2×10^{-5}	4.2
i-C_4H_{10} ox.[d]	Pt–Pt	10.8	0.275	−5.2	4.1×10^{-5}	1.1
i-C_4H_8 ox.[a]	Pt–Pt	11.5	0.277	−1.9	3.4×10^{-5}	0.4
H_2 red.[c]	Pt–Pt	6.1	0.274	−5.2	6.5×10^{-5}	4.8
	Pt–Sb	0.6	0.260	8.9	5.1×10^{-5}	
Pt foil[d]						
(model compound)	Pt–Pt	12.0	0.278	0.0	3.6×10^{-5}	—

Note. Selective oxidation reaction conditions: 2400 ml h^{-1}; 20% *i*-C_4H_{10} or 1.7% *i*-C_4H_8, 4% O_2, balanced with He.

[a] FT range: 25–135 nm^{-1}, FF range: 0.18–0.33 nm.
[b] FT range: 25–170 nm^{-1}, FF range: 0.20–0.30 nm.
[c] FT range: 25–160 nm^{-1}, FF range: 0.17–0.35 nm.
[d] FT range: 25–180 nm^{-1}, FF range: 0.17–0.33 nm.
[e] ±0.7.
[f] ±0.001 nm.

photographs of Fig. 7 showed that the surface of the SbO_x looked very rough like porous materials.

The Pt particles seemed to be more sparse for 0.5 wt% Pt/SbO_x than 2.0 wt% Pt/SbO_x. For the 0.5 wt% Pt/SbO_x sample, Pt particles gradually appeared with time for the

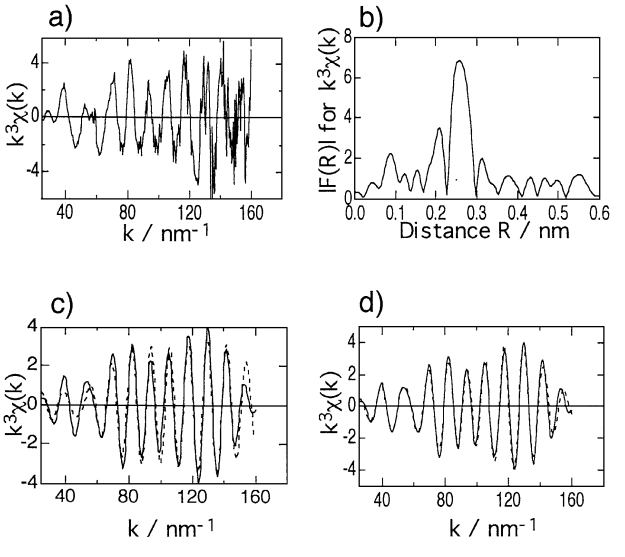

FIG. 6. The EXAFS curve fitting procedure for 2.0 wt% Pt/SbO_x reduced with H_2 at 473 K: (a) EXAFS oscillation; (b) its associated Fourier transform; (c) one-shell (Pt–Pt) fitting; (d) two shells (Pt–Pt and Pt–Sb) fitting.

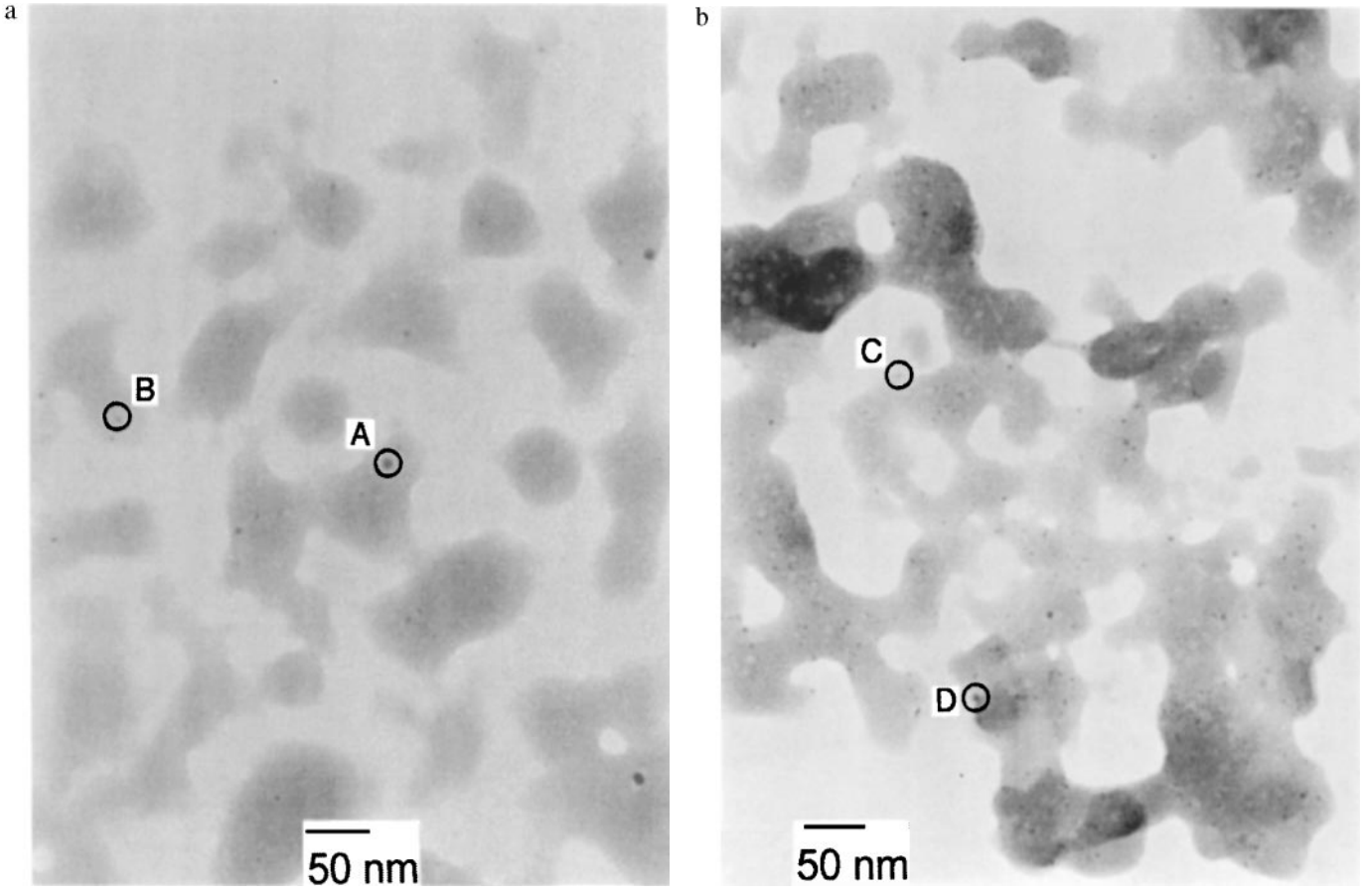

FIG. 7. TEM images (magnification, 350,000) of (a) Pt/SbO_x (0.5 wt%) and (b) Pt/SbO_x (2.0 wt%) calcined at 773 K.

observation by TEM; in other words, Pt particles were detectable after a part of the SbO_x was sublimated by electron beams. The contrasted images, A–D, in Figs. 7a and b were characterized by EDX analysis in Fig. 8, which proves that they are Pt particles. The EDX analysis cannot provide information of whether these particles are pure Pt particles or Pt particles modified by Sb, because of lots of Sb support.

Size distributions of Pt particles in both 0.5 and 2.0 wt% Pt/SbO_x are shown in Figs. 9a and b, respectively. The average particle sizes were estimated as 5.5 and 3.7 nm for 0.5 wt% Pt/SbO_x and 2.0 wt% Pt/SbO_x, respectively. These values are compatible with the ones derived from XRD.

DISCUSSION

The XRD (Fig. 1), EXAFS (Fig. 4 and Table 3), and TEM (Figs. 7 and 8) data demonstrate that Pt in the Pt/SbO_x catalysts forms metallic particles after the calcination at 773 K. The coordination numbers of Pt–Pt (0.275–0.277 nm) in 0.5 wt% Pt/SbO_x and 2.0 wt% Pt/SbO_x were as large as 10.3 and 11.8, respectively, which are close to that for bulk Pt (12.0). Thus there is no evidence for the coexistence of isolated Pt ions and Pt oxides in the calcined samples. The small increase in the white line peaks in the XANES spectra for 0.5 and 2.0 wt% Pt/SbO_x calcined at 773 K (Fig. 3) may be due to adsorption of oxygen on the Pt surface. The presence of adsorbed oxygen is also suggested in H_2 adsorption measurements; the amount of adsorbed hydrogen (Pt–H) in the first run assuming $Pt{-}O + 3H \rightarrow Pt{-}H + H_2O$ agreed with that measured in the second run after evacuation of the sample at 473 K after the first run, as shown in Table 1.

Pt dispersion is usually controlled by the loading; that is, the more Pt loaded on SbO_x, the larger Pt particles would grow. The H/Pt values in Table 1 indicate an opposite tendency. The Pt particle sizes for 0.5 wt% Pt/SbO_x and 2.0 wt% Pt/SbO_x were calculated to be 13.0 and 5.2 nm, respectively, assuming a spherical shape of the particles (Table 4). The mean Pt particle sizes (Table 4) estimated by the particle size distribution in TEM (Fig. 9) were 5.5 and 3.7 nm for the 0.5 and 2.0 wt% Pt/SbO_x catalysts, respectively, which also show that the Pt particles on SbO_x are larger with the less Pt loading sample. The Pt particle sizes were also calculated to be 6.4 and 3.5 nm for the Pt/SbO_x catalysts with Pt loadings of 0.5 and 2.0 wt%, respectively from the broadening of the XRD Pt(111) peaks in Fig. 1, although the XRD patterns were noisy due to the low Pt

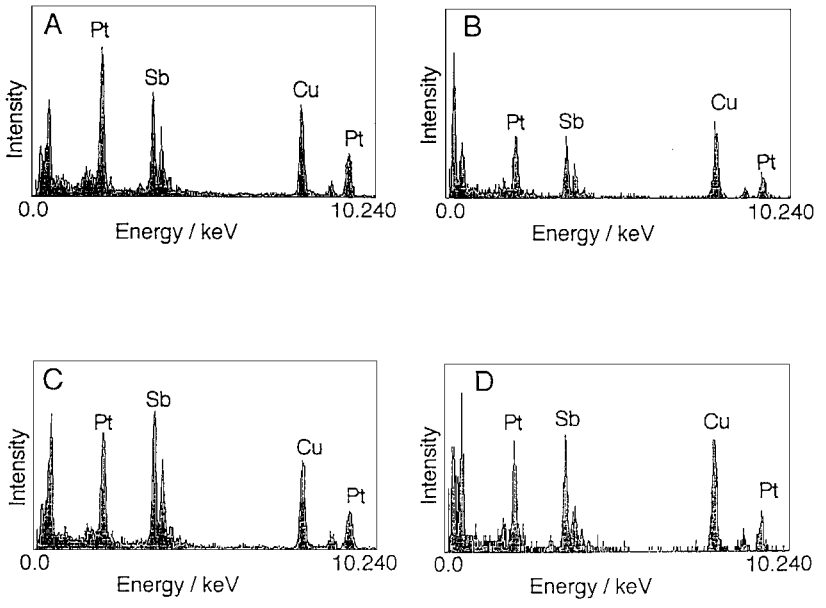

FIG. 8. EDX analysis for the particles A–D in the TEM images of Fig. 7.

loadings. The coordination numbers of Pt–Pt (10.3–11.8) in EXAFS also provide the particle sizes ≥4.0 nm, although the values in this range could not be evaluated precisely by EXAFS. There is difference in Pt particle sizes determined by H/Pt, XRD, TEM, and EXAFS. The Pt particle sizes in Pt/SbO_x catalysts estimated from H/Pt were 1.5–2 times larger than the values derived from XRD, TEM, and EXAFS. The results that the H/Pt values are much smaller than those expected from the XRD, TEM, and EXAFS data imply that the surface property of Pt particles in the calcined Pt/SbO_x catalysts is different from that of Pt metal. This is also suggested by the CO adsorption measurements in Table 1, where the adsorption of CO (CO/Pt) was remarkably suppressed. The suppression of H_2 and CO adsorption may be due to the decoration effect of SbO_y ($y < x$) like the SMSI (strong metal–support interaction) (25).

To examine the interaction between Pt and SbO_x we measured the Pt(111) XRD lines and the EXAFS spectra for the Pt/SbO_x catalysts under more reducible conditions. The Pt(111) diffraction peak drastically decreased after i-C_4H_8 oxidation reaction (4% i-C_4H_8, 4% O_2, balanced with He) at 773 K and reduction with H_2 at 473 K as shown in Fig. 1. The structural change in Pt particles was also observed in the EXAFS oscillation for the Pt/SbO_x sample reduced with H_2 at 473 K as shown in Fig. 4Be. The careful EXAFS analysis by a curve-fitting technique revealed the presence of Pt–Sb bond at 0.260 nm besides Pt–Pt bond at 0.274 nm (Fig. 6 and Table 3), demonstrating the formation of Pt–Sb alloy in the reduced Pt/SbO_x catalysts. After the i-C_4H_8 oxidation reactions (1.7% i-C_4H_8 or 4% i-C_4H_8, 4% O_2, balanced with He) at 773 K the Pt–Sb bonding was not able to be observed by EXAFS, where only Pt–Pt bonds with large Pt–Pt coordination numbers similar to those for the calcined Pt/SbO_x catalysts were observed in Table 3. To explain both results of XRD in Fig. 1c and EXAFS in Table 3, we propose that the Pt–Sb alloy formation proceeds from the surface of the Pt particles. The Pt–Sb alloy phase near

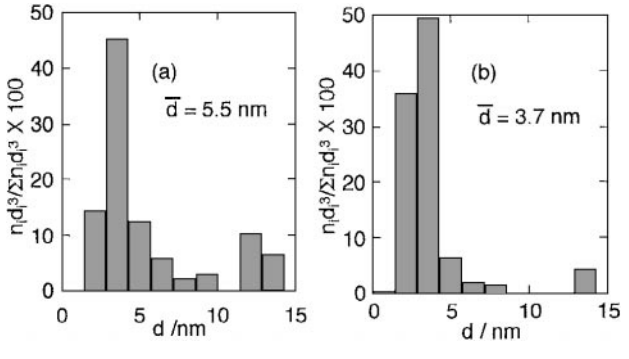

FIG. 9. Size distribution of Pt particles in (a) Pt/SbO_x (0.5 wt%) and (b) Pt/SbO_x (2.0 wt%) derived from the TEM images.

TABLE 4

Comparison of Pt Particle Sizes in Pt/SbO_x Evaluated by H/Pt, XRD, TEM, and EXAFS

	Pt particle size/nm		
Pt loading	0.5 wt%	1.0 wt%	2.0 wt%
H/Pt	13	12	5.2
XRD	6.4	—	3.5
TEM	5.5	—	3.7
EXAFS	≥4.0	—	≥4.0

the surface could not be detected by EXAFS. The degree of the alloy formation in the Pt particles depends on the atmosphere. The XRD for the sample after the *i*-C_4H_8 selective oxidation at the low concentration of *i*-C_4H_8 (1.7%) showed a similar XRD pattern to Figs. 1a and b. While under the catalytic *i*-C_4H_8 (1.7%) selective oxidation the bulk data of XRD and EXAFS exhibit metallic Pt particles, the adsorption of H_2 and CO was suppressed to nearly zero level (Table 2), demonstrating modification of the Pt surface probably by SbO_y as mentioned above.

As for the Pt/SbO_x catalyst after the *i*-C_4H_{10} selective oxidation to MAL (20% *i*-C_4H_{10}, 4% O_2, balanced with He) at 773 K, the XRD and EXAFS data were similar to those for the calcined catalyst before the catalytic reactions (Figs. 1, 3, 4, and 5). These results from the bulk characterization indicate that the Pt particles remained essentially unchanged after *i*-C_4H_{10} oxidation. However, the drastic decrease in H_2 adsorption was observed with Pt/SbO_x after *i*-C_4H_{10} oxidation as shown in Table 2. The feature is similar to that for Pt/SbO_x reduced with H_2 and after the *i*-C_4H_8 oxidation reaction (*i*-$C_4H_8 \geq 4\%$), where at least the surface layers of Pt particles form on alloy with Sb. It is to be noted that Pt and Sb tend to make alloy particles on SbO_x with each other under reducing conditions. However, under the reaction condition of the *i*-C_4H_{10} selective oxidation, Sb on the Pt surface should be partially oxidized. Raman study indicated small Sb_2O_3 oxide crystallites forming on or around Pt particles, with small highly dispersed antimony species, possibly O=SbO_z decorating the surface (14).

As mentioned above, hydrogen adsorption decreased on the calcined Pt/SbO_x catalysts, whereas CO adsorption was more drastically suppressed (Table 1). This is contrasted to the case of Pt–Sn and Rh–Sn/SiO_2 catalysts (11, 12, 24, 26), where H_2 adsorption was suppressed more than CO adsorption. The large reduction in CO adsorption on the calcined Pt/SbO_x catalyst is explained by site block and dilution effect by the Sb suboxide species at the Pt particle surface, while the small effect of the Sb suboxides on H_2 adsorption cannot be referred to the same reason. H_2 may be heterolytically dissociated by a synergistic mechanism on Pt–SbO_y sites.

The antimony oxide was transformed to Sb_6O_{13} under the calcination condition as shown in Fig. 2, which is consistent with the previous study (27). On the calcined Pt/SbO_x catalysts *i*-C_4H_{10} was selectively oxidized to MAL (13, 15). Under the reducible conditions such as the *i*-C_4H_8 rich (20%) reaction condition, the Sb_6O_{13} phase was further reduced to α-Sb_2O_4 phase, where the selectivity to MAL reduced to less than 20%. On the Pt/α-Sb_2O_4 the complete oxidation to CO_2 was predominant. Thus it seems that the high selectivity to MAL in the *i*-C_4H_{10} oxidation is attained when the Pt surface modified by Sb suboxides (Sb_2O_3 and possibly O=SbO_z) are formed on the Sb_6O_{13} support as illustrated in Fig. 10a.

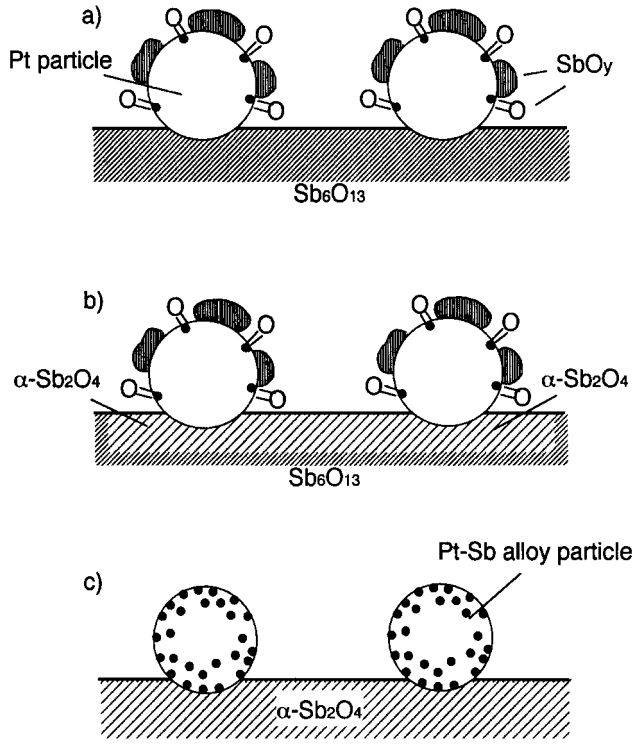

FIG. 10. Selective phase (a), nonselective phase (b), and reduced phase (c) of the Pt/SbO_x catalyst for the oxidation reaction of *i*-C_4H_{10} to MAL, proposed by XRD, TEM, XAFS, and gas adsorption.

Sb_6O_{13} has been regarded as a defect pyrochlore-type structure, which has Sb^{5+}–O–Sb^{5+} zigzag chains along the [110] axis (27, 28). The Sb^{5+}–O–Sb^{5+} chains in Sb_6O_{13} may be responsible for selective oxidation of unsaturated hydrocarbons like *i*-C_4H_8 (1, 29). On the contrary, α-Sb_2O_4 phase has been demonstrated to work as "donor" which supplies reactive oxygen atoms on active sites (30). Extreme reaction condition leads to the formation of α-Sb_2O_4 and total oxidation as shown in Fig. 10b.

CONCLUSIONS

(1) We have characterized a new Pt/SbO_x catalyst, active for the selective oxidation of *i*-C_4H_{10} and *i*-C_4H_8 to MAL with high selectivities, by means of XRD, TEM, XAFS, and gas adsorption.

(2) In the selective Pt/SbO_x catalyst the Sb oxide is transformed to Sb_6O_{13} phase.

(3) The Pt particle surface is modified by Sb suboxides (Sb_2O_3 and possibly O=SbO_z) under the catalytic selective oxidation reaction conditions, which is relevant to suppression of the total oxidation and the selective dehydrogenation of *i*-C_4H_{10} to *i*-C_4H_8 and *i*-C_4H_7 (methallyl species) or of *i*-C_4H_8 to *i*-C_4H_7.

(4) The Sb_6O_{13} phase is responsible for the selective oxidation step of *i*-C_4H_8 and *i*-C_4H_7 to MAL.

(5) Too heavy reduction of the catalyst leads to the formations of Pt–Sb alloy particles and α-Sb_2O_4 which enhances the total oxidation to CO_2.

ACKNOWLEDGMENT

This work has been supported by CREST (Core Research for Evolutional Science and Technology) of Japan Science and Technology Corporation (JST).

REFERENCES

1. Centi, G., Grasselli, R. K., and Trifirò, F., *Catal. Today* **13**, 661 (1992).
2. Centi, G., *Catal. Lett.* **22**, 53 (1993).
3. Centi, G., Trifirò, F., Ebner, J. R., and Franchetti, V. M., *Chem. Rev.* **88**, 55 (1988).
4. Grasselli, R. K., and Burrington, J. D., *Adv. Catal.* **30**, 133 (1981).
5. Moro-oka, Y., and Ueda, W., *Adv. Catal.* **40**, 233 (1994).
6. Catani, R., Centi, G., Trifirò, F., and Grasselli, R. K., *Ind. Eng. Chem. Res.* **31**, 107 (1992).
7. Kim, Y.-C., Ueda, W., and Moro-oka, Y., *Appl. Catal.* **70**, 189 (1991).
8. Hatano, M., and Kayo, A. (Mitsubishi Kasei Corp.), Europ. Pat. 318, 295 (1991).
9. Ushikubo, T., Oshima, K., Kayo, A., Umezawa, T., Kiyono, K., and Sawaki, I. (Mitsubishi Kasei Corp.), Europ. Pat. 529, 853 (1993).
10. Bettahar, M. M., Costentin, G., Savary, L., and Lavalley, J. C., *Appl. Catal. A: General* **145**, 1 (1996).
11. Inoue, T., Tomishige, K., and Iwasawa, Y., *J. Chem. Soc., Chem. Commun.* **1995**, 329 (1996).
12. Inoue, T., Tomishige, K., and Iwasawa, Y., *J. Chem. Soc., Faraday Trans.* **92**, 461 (1996).
13. Inoue, T., Asakura, K., and Iwasawa, Y., *Shokubai (Catalysts and Catalysis)* **38**, 502 (1996).
14. Inoue, T., Asakura, K., Li, W., Oyama, S. T., and Iwasawa, Y., *Appl. Catal.*, in press.
15. Inoue, T., Asakura, K., and Iwasawa, Y., *J. Catal.*, in press.
16. Scherrer, P., *Göttinger Nachr.* **2**, 98 (1918).
17. Liu, T., Asakura, K., Lee, U., Matsui, Y., and Iwasawa, Y., *J. Catal.* **135**, 367 (1992).
18. Teo, B. K., *in* "EXAFS: Basic Principle and Data Analysis," p. 26, Springer-Verlag, New York, 1986.
19. Asakura, K., *in* "X-ray Absorption Fine Structure for Catalysts and Surfaces" (Y. Iwasawa, Ed.), p. 33, World Scientific, Singapore, 1996.
20. Rehr, J. J., Mustre de Leon, J., Zabinsky, S. I., and Albers, R. C., *J. Am. Chem. Soc.* **113**, 5135 (1991).
21. Stern, E. A., *Phys. Rev. B* **48**, 9825 (1993).
22. Greegor, R. B., and Lytle, F. W., *J. Catal.* **63**, 476 (1980).
23. Caballero, A., Dexpert, H., Didillion, B., LePeltier, F., Clause, O., and Lynch, J., *J. Catal.* **97**, 11283 (1993).
24. Tomishige, K., Asakura, K., and Iwasawa, Y., *J. Catal.* **149**, 70 (1994).
25. Haller, G. L., and Resasco, D. E., *Adv. Catal.* **36**, 173 (1989).
26. Tomishige, K., Asakura, K., and Iwasawa, Y., *J. Catal.* **157**, 472 (1995).
27. Stewart, D. J., Knop, O., Ayasse, C., and Woodhams, F. W. D., *Can. J. Chem.* **50**, 690 (1972).
28. Jona, F., Shirane, G., and Pepinsky, R., *Phys. Rev.* **98**, 903 (1955).
29. Burrington, J. D., Kartisek, C. T., and Grasselli, R. K., *J. Catal.* **87**, 363 (1984).
30. Delmon, B., and Froment, G. F., *Catal. Rev.-Sci. Eng.* **38**, 69 (1996).